Tristable flow states and reversal of the large-scale circulation in two-dimensional circular convection cells

Ao Xu[1], Xin Chen[1] and Heng-Dong Xi[1]†

[1]School of Aeronautics, Northwestern Polytechnical University, Xi'an 710072, China

We present a numerical study of the flow states and reversals of the large-scale circulation (LSC) in a two-dimensional (2D) circular Rayleigh-Bénard cell. Long-time direct numerical simulations are carried out for the Rayleigh number (Ra) of $10^7 \leqslant Ra \leqslant 10^8$ and the Prandtl number (Pr) of $2.0 \leqslant Pr \leqslant 20.0$. We found that a new, long-lived, chaotic flow state exists, in addition to the commonly observed circulation states (the LSC in the clockwise and counterclockwise directions). The circulation states consist of one primary roll in the middle and two secondary rolls near the top and bottom circular walls. The primary roll becomes stronger and larger, while the two secondary rolls diminish, with increasing Ra. Our results suggest that the reversal of the LSC is accompanied by that the secondary rolls grow, break the primary roll, and then connect to form a new primary roll with reversed direction. We mapped out the phase diagram of the existence of the LSC and the reversal on Ra and Pr, which reveals that the flow is in the circulation states when Ra is large and Pr is small. The reversal of the LSC can only occur in a limited Pr range. The phase diagram can be understood in terms of competition between the thermal and viscous diffusions. We also found that the internal flow states manifested themselves into global properties such as Nusselt and Reynolds numbers.

Key words: Bénard convection, plumes/thermals, turbulent convection

1. Introduction

Spontaneous flow reversals occur widely in astrophysical and geophysical systems, such as reversals of the convective wind in the atmosphere (van Doorn *et al.* 2000; Gallet *et al.* 2012) and reversals of the convective flow in the Earth or stars (Glatzmaier *et al.* 1999; Miesch & Toomre 2009; Pétrélis *et al.* 2009; Biggin *et al.* 2012). A paradigm to study the mechanism of the flow reversals is the Rayleigh-Bénard (RB) convection, which is a fluid layer heated from the bottom and cooled from the top (Ahlers *et al.* 2009; Lohse & Xia 2010; Chillà & Schumacher 2012; Xia 2013). The control parameters of the system include the Rayleigh number $Ra = \alpha g \Delta_T H^3/(\nu\kappa)$, which describes the strength of buoyancy force relative to thermal and viscous dissipative effects; and the Prandtl number $Pr = \nu/\kappa$, which describes the thermophysical fluid properties. Here, α, κ and ν are the thermal expansion coefficient, thermal diffusivity, and kinematic viscosity of the fluid, respectively; g is the gravitational acceleration, and $\Delta_T = T_{\text{hot}} - T_{\text{cold}}$ is the temperature difference across the fluid layer of height H. At sufficiently high Ra, a

† Email address for correspondence: hengdongxi@nwpu.edu.cn

large-scale circulation (LSC) that spans the size of the convection cell is established (Krishnamurti & Howard 1981; Cioni *et al.* 1997), which essentially results from the organization of thermal plume motion due to plume-vortex and plume-plume interactions (Xi *et al.* 2004; Zhou & Xia 2010). An interesting feature of the LSC is the spontaneous and random reversal of its flow direction (Sreenivasan *et al.* 2002; Brown *et al.* 2005; Brown & Ahlers 2006; Xi & Xia 2007, 2008*a*; Xiao *et al.* 2018). To minimize or even eliminate the influence from the three-dimensional complex dynamic features of the LSC in cylindrical cells (Funfschilling & Ahlers 2004; Xi *et al.* 2009) and in cubic cells (Kaczorowski & Xia 2013), a two-dimensional (2D) or quasi-2D square cell was used to study the reversal of the LSC (Xia *et al.* 2003; Sugiyama *et al.* 2010; Wagner & Shishkina 2013), in which the LSC is confined within the 2D or quasi-2D plane, while the flow switches between a clockwise circulation state and a counterclockwise circulation state. During the reversal process, the corner rolls play a crucial role (Sugiyama *et al.* 2010). They grow in size and kinetic energy to weaken and eventually break up the primary circulating roll. After that, two corner rolls connect to form a new primary roll again, but with a reversed circulating direction (Sugiyama *et al.* 2010; Chandra & Verma 2013). Recently, it was shown that in the quasi-2D square cells, the corner roll is not necessary for the occurrence of reversals. The probability of the occurrence of reversals mainly depends on the stability of the LSC itself. The role of the corner roll is to destabilize the LSC, thus increasing the reversal frequency (Chen *et al.* 2019, 2020).

To eliminate the effect of corner rolls on the reversals of the LSC, Wang *et al.* (2018*b*) conducted experiments in a quasi-2D cell with its circular plane oriented parallel to the gravity (referred to as vertical circular thin disk from now on). The top one-third and bottom one-third of the circular sidewalls are kept at low and high temperatures, respectively; the left and right sidewalls, each is one-sixth of the whole circular wall, are made of thermal insulating Plexiglas (Song *et al.* 2011, 2014; Wang *et al.* 2018*b*,*c*). The shape of their specially designed cell matches the single-roll structure of the LSC perfectly; thus, there are no corner rolls to destabilize the LSC. Through visualization of the LSC and plume dynamics, Wang *et al.* (2018*b*) proposed that the reversal of the LSC is due to that the rare massive eruption of thermal plumes disrupt the existing LSC and reset its rotational direction. The massive eruption was attributed to boundary layer instability induced by continuous heat accumulation or spontaneous fluctuations in turbulent thermal convection (Wang *et al.* 2018*b*). However, a general understanding of the reversal mechanism remains elusive.

In this paper, inspired by the experimental study in the vertical circular thin disk by Wang *et al.* (2018*b*), we present a numerical study of the flow topology and reversal of the LSC in a 2D circular cell with its circular plane orientated parallel to gravity. Long-time direct numerical simulations with at least 100 000 free-fall time units were performed for the Rayleigh number of $10^7 \leqslant Ra \leqslant 10^8$, and the Prandtl number of $2.0 \leqslant Pr \leqslant 20.0$. We found that in addition to the commonly observed circulation state (namely, the LSC), the flow spends a considerable long time in a chaotic state where the plumes go up and down randomly. This newly observed chaotic state prevails at low Ra while the circulation state prevails at high Ra. We also mapped out the phase diagram of the existence of the LSC and its reversal on the Ra-Pr plane. The rest of this paper is organized a follows: In Section 2, we present the numerical details for the simulations. In Section 3, general flow and heat transfer features in the 2D circular cell are presented, and the dynamics of the novel tristable flow states in the circular cell are introduced; after that, the Fourier mode decomposition analysis is adopted to understand the effects of Ra and Pr on the flow states. In Section 4, the main findings of the present work are summarized.

2. Numerical method

2.1. *Direct numerical simulation of incompressible thermal flows*

We consider the incompressible thermal flows under the Boussinesq approximation: the temperature is treated as an active scalar, and its influence on the velocity field is realized through the buoyancy term; all the transport coefficients are assumed to be constants. The governing equations can be written as

$$\nabla \cdot \mathbf{u} = 0 \tag{2.1}$$

$$\frac{\partial \mathbf{u}}{\partial t} + \mathbf{u} \cdot \nabla \mathbf{u} = -\frac{1}{\rho_0} \nabla p + \nu \nabla^2 \mathbf{u} + g\alpha(T - T_0)\hat{\mathbf{y}} \tag{2.2}$$

$$\frac{\partial T}{\partial t} + \mathbf{u} \cdot \nabla T = \kappa \nabla^2 T \tag{2.3}$$

where $\mathbf{u} = (u, v)$ is the fluid velocity. p and T are pressure and temperature of the fluid, respectively. ρ_0 and T_0 are reference density and temperature, respectively. $\hat{\mathbf{y}}$ is the unit vector in vertical direction.

We adopt the lattice Boltzmann (LB) method as the numerical tool to solve the above equations. The advantages of the LB method include easy implementation and parallelization as well as low numerical dissipation (Chen & Doolen 1998; Aidun & Clausen 2010; Xu *et al.* 2017*b*). In this work, the LB method is based on a double distribution function approach, which consists of a D2Q9 discrete velocity model for the Navier-Stokes equations to simulate fluid flows (i.e., solving Eqs. 2.1 and 2.2) and a D2Q5 discrete velocity model for the convection-diffusion equation to simulate heat transfer (i.e., solving Eq. 2.3). To simulate fluid flows and heat transfer in the circular domain, we apply the interpolated bounce-back scheme at the curved wall. Specifically, to guarantee no-slip velocity boundary conditions at the curved wall, we apply the interpolated bounce-back scheme by Bouzidi *et al.* (2001) for the density distribution function; to achieve the Dirichlet or Neumann temperature boundary conditions at the curved wall, we apply the interpolated bounce-back scheme by Li *et al.* (2013) for the temperature distribution function. More numerical details on the LB method and validation of the in-house code can be found in our previous work (Xu *et al.* 2017*a*, 2019*a*,*b*).

2.2. *Simulation settings*

As illustrated in figure 1, the top (blue curve) and the bottom (red curve) one-third of the circular walls are kept at constant low and high temperature of T_{cold} and T_{hot}, respectively, while the left and right one-sixth of the circular sidewalls (black curves) are adiabatic. All circular walls impose no-slip velocity boundary conditions. The diameter of the circular cell is D and is chosen as the characteristic length of the system. Simulation results are provided for Rayleigh number $Ra = \alpha g \Delta_T D^3/(\nu\kappa)$ of $10^7 \leqslant Ra \leqslant 10^8$, and Prandtl number of $2.0 \leqslant Pr \leqslant 20.0$. To have better statistics, we run each simulation for at least 100 000 t_f, and in some cases, the simulation times are as long as 200 000 t_f. Here, t_f denotes free-fall time units $t_f = \sqrt{D/(g\alpha\Delta_T)}$. We also check whether the grid spacing Δ_g and time interval Δ_t are adequately resolved by comparing it with the Kolmogorov and Batchelor scales. Here, we roughly estimate the global kinetic energy dissipation rate as $\langle \varepsilon_u \rangle = RaPr^{-2}(Nu-1)\nu^3/D^4$ (Shraiman & Siggia 1990), thus, the Kolmogorov length scale can be estimated by the global relation as $\eta_K = (\nu^3/\langle\varepsilon_u\rangle)^{1/4} = DPr^{1/2}/[Ra(Nu-1)]^{1/4}$, the Batchelor length scale can be estimated as $\eta_B = \eta_K Pr^{-1/2}$ (Silano *et al.* 2010), and the Kolmogorov time scale can be estimated as $\tau_\eta = \sqrt{\nu/\langle\varepsilon_u\rangle} = t_f\sqrt{Pr/(Nu-1)}$. The global heat transport is measured by the wall-averaged Nusselt number as $Nu =$

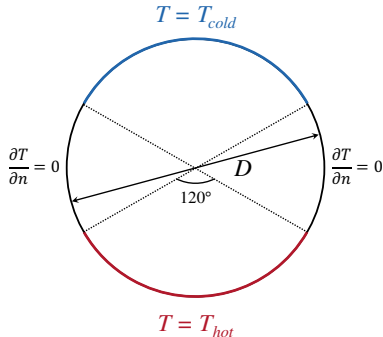FIGURE 1. Schematic illustration of the 2D circular convection cell.

Ra	Pr	D	Δ_g/η_K	Δ_g/η_B	$\Delta_t/\tau_\eta \times 10^3$
1.0×10^7	[2.0, 20.0]	257	[0.10, 0.29]	[0.41, 0.43]	[3.4, 9.5]
2.0×10^7	[2.0, 20.0]	385	[0.08, 0.24]	[0.34, 0.36]	[2.5, 7.0]
3.0×10^7	[2.0, 20.0]	385	[0.09, 0.27]	[0.38, 0.41]	[2.7, 7.3]
4.5×10^7	[2.0, 20.0]	385	[0.10, 0.31]	[0.44, 0.47]	[2.8, 7.9]
6.0×10^7	[2.0, 20.0]	513	[0.09, 0.26]	[0.36, 0.38]	[2.2, 6.2]
8.0×10^7	[2.0, 20.0]	513	[0.09, 0.28]	[0.40, 0.42]	[2.3, 6.6]
1.0×10^8	[2.0, 20.0]	513	[0.10, 0.31]	[0.43, 0.45]	[2.4, 6.9]

TABLE 1. Spatial and temporal resolutions of the simulations.

$-(\langle\partial_\mathbf{n} T\rangle_{\text{top},t} + \langle\partial_\mathbf{n} T\rangle_{\text{bottom},t})/2$, where $\langle\cdots\rangle_{\text{top/bottom},t}$ denotes the ensemble average over the top (or bottom) one-third of the circular walls and over the time (Kerr 1996; Verzicco & Camussi 2003), $\mathbf{n}$ denotes the unit vector in the wall norm direction. From table 1, we can see that grid spacing satisfies the criterion of $\max(\Delta_g/\eta_K, \Delta_g/\eta_B) \leqslant 0.47$, which ensures spatial resolution. Besides, the time intervals are $\Delta_t \leqslant 0.0095\tau_\eta$, thus, adequate temporal resolution is guaranteed.

3. Results and discussion

3.1. *Global flow and heat transfer features*

We first examine the scaling of the global quantities, such as Nusselt number (Nu) and Reynolds number (Re), on the control parameter Ra. The measured Nu and Re as a function of Ra are shown in figures 2(a) and 2(b), respectively. Due to zero value of the averaged velocity over the whole cell, we choose the root-mean-square velocity $u_{rms} = \sqrt{\langle(u^2 + v^2)\rangle_{V,t}}$ as the characteristic velocity to calculate the Reynolds number $Re = u_{rms}D/\nu$ (Sugiyama *et al.* 2009). Here, $\langle\cdots\rangle_{V,t}$ denotes the volume and time average. The data shown in figure 2 can be described by power-law relations for each Pr, namely, $Nu \propto Ra^\beta$ and $Re \propto Ra^\gamma$. To further confirm the data faithfully follow the power-law, we show the compensated plots of Nu and Re as a function of Ra in figures 2(c) and 2(d), respectively. The heat transfer scaling exponent β ranges between 0.26 and 0.30 for various Pr, while the momentum scaling exponent γ ranges between 0.52 and 0.67. The $Nu(Ra)$ and $Re(Ra)$ scaling exponents in the 2D circular cell are close to that in the 2D (or quasi-2D) square cell, where $\beta = 0.285 \sim 0.30$ (Ciliberto *et al.* 1996; van der Poel *et al.* 2012; Huang & Xia 2016; Zhang *et al.* 2017) and $\gamma = 0.59 \sim 0.62$ (Xia *et al.* 2003; Sun & Xia 2005; Zhou *et al.* 2007; van der Poel *et al.* 2012; Zhang *et al.*
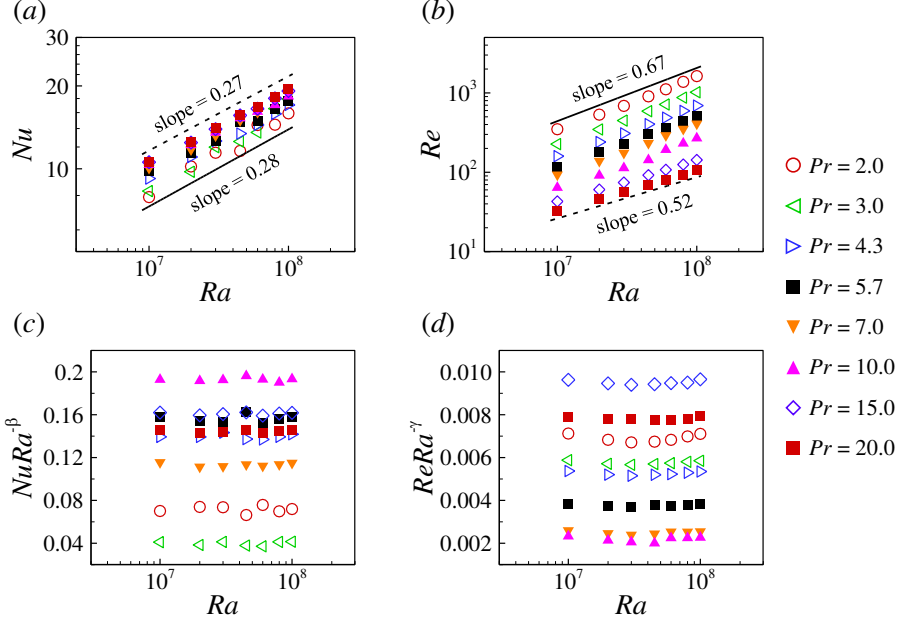
FIGURE 2. (*a*) Nusselt number and (*b*) Reynolds number, (*c*) compensated plots of Nusselt number and (*d*) compensated plots of Reynolds number as a function of Rayleigh number for various Prandtl numbers.

2017) for moderate Pr. In addition, the heat transfer scaling exponent β from our simulations ($\beta = 0.26$ for $Pr = 4.3$ and $\beta = 0.25$ for $Pr = 5.7$) are very close to experimental measurements (Song *et al.* 2011, 2014; Wang *et al.* 2018*b,c*) in the quasi-2D circular cell ($\beta = 0.275$ for $Pr = 4.4$ and $\beta = 0.28$ for $Pr = 5.4$). The differences in the momentum scaling exponent γ, namely, $\gamma = 0.64$ for $Pr = 5.7$ from our simulations compared with $\gamma = 0.49$ for $Pr = 5.4$ from experimental measurements (Song *et al.* 2011, 2014; Wang *et al.* 2018*b,c*), are due to stronger strength of the convection in two dimension than that in three dimension (van der Poel *et al.* 2013). Overall, the global heat transfer and momentum quantities reveal the simulated system possesses the key features of turbulent convection.

3.2. *The tristable flow state and reversal of the large-scale circulation*

To study the time evolution of the flow topology, we calculate the global angular momentum $L(t) = \langle -(y - D/2)u(\mathbf{x}, t) + (x - D/2)v(\mathbf{x}, t) \rangle_V$ of the flow field, where $\langle \cdots \rangle_V$ denotes the volume average. Previously, it was shown that the global angular momentum could nicely indicate different flow states in the 2D circular cell (Sugiyama *et al.* 2010). Figure 3(a) shows the time series of the dimensionless global angular momentum $L(t)/L_0$ at $Ra = 10^7$ and $Pr = 4.3$ for the period of 50 000 free-fall time. Here, L_0 is the maximum of the absolute value of $L(t)$. We can see from figure 3(a) that L switches between three meta-stable states: one state with positive fluctuating L well above zero, which corresponds the LSC in the clockwise direction (referred to as CLSC), one state with negative fluctuating L well below zero, which corresponds the LSC in the counterclockwise direction (referred to as CCLSC), and one state with L fluctuating around zero, which is referred to as chaotic state with random motion of plumes. The tristable flow states are much clearer in figure 3(b), where an enlarged view of the time segments of $L(t)/L_0$ is shown. We use the following four pairs of symbols to denote the
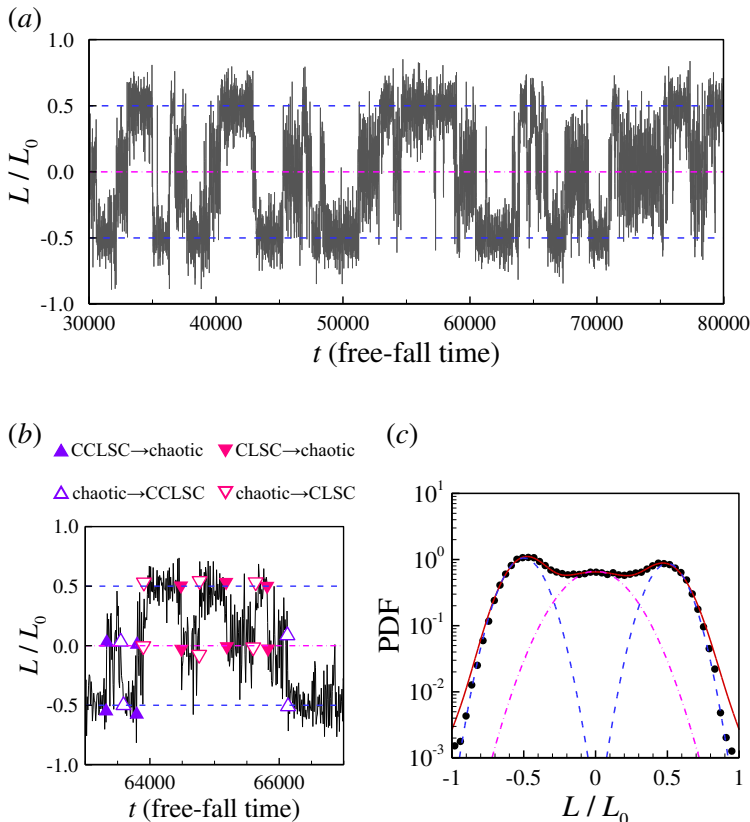
FIGURE 3. (*a*) Time trace of the global angular momentum L of the flow for $Ra = 10^7$ and $Pr = 4.3$ (nondimensionalized by its maximum value L_0); (*b*) Enlarged one portion of the data shown in (*a*) to illustrate the tristable state; (*c*) The probability density function (PDF) of the dimensionless global angular momentum, the three dashed lines are the fitting of the data to the three independent Gaussian functions, while the solid line is the fitting of the data to a triple-Gaussian function.

flow states transitions: i) up filled triangles mark the transitions from the CCLSC to chaotic states, ii) up hollow triangles mark the transitions from the chaotic to CCLSC states, iii) down filled triangles mark the transitions from the CLSC to chaotic states, and iv) down hollow triangles mark the transitions from the chaotic to CLSC states. The tristable behaviour of the flow state can also be seen from the probability density functions (PDFs) of $L(t)/L_0$ shown in figure 3(c). The three dashed lines are the fitting results using three independent Gaussian functions, while the solid line is the fitting result using the triple-Gaussian function. The most probable values of $L(t)/L_0$ for these three states are around ± 0.5 and 0, respectively. This tristable flow state feature is distinguishable from the bistable behaviour in 2D or quasi-2D square cells, where the LSC switches only between CLSC and CCLSC, and a double-Gaussian function best fits the PDFs of the flow strength in terms of either global angular momentum or the temperature contrast (Sugiyama *et al.* 2010; Chandra & Verma 2011; Ni *et al.* 2015; Huang & Xia 2016; Castillo-Castellanos *et al.* 2016, 2019).

Typical snapshots of temperature and velocity fields for the three meta-sable flow states at $Ra = 10^7$ and $Pr = 4.3$ are shown in figures 4(a-c), and the corresponding video can be viewed in the supplementary movie 1. From the video and snapshots, we
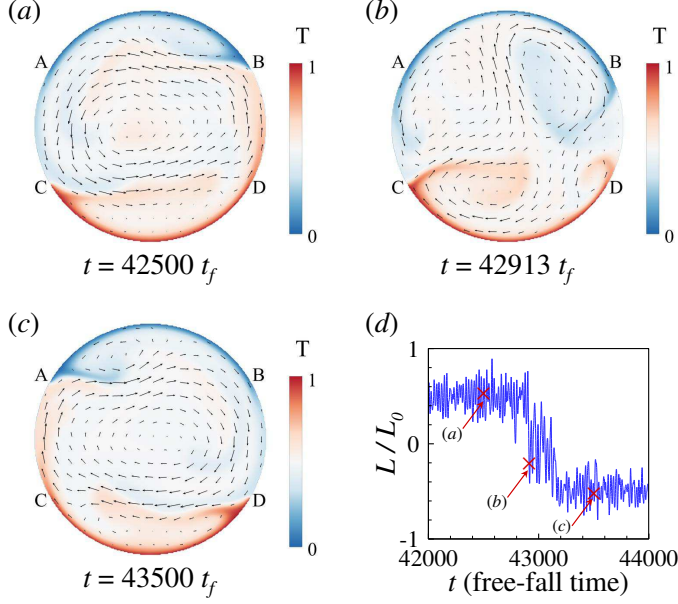
FIGURE 4. Typical snapshots of temperature field (contour) and velocity field (arrows) of the flow field at (*a*) $t = 42500 \ t_f$, (*b*) $t = 42913 \ t_f$, and (*c*) $t = 43500 \ t_f$; (*d*) Time segment of the dimensionless global angular momentum $L(t)/L_0$. The flow fields and $L(t)/L_0$ are obtained at $Ra = 10^7$ and $Pr = 4.3$. Arcs $\widehat{AB}$ and $\widehat{CD}$ denote the top and bottom one-third circular walls, respectively.

can identify the two circulation states, namely, both the CCLSC and CLSC (see figures 4a and 4c, respectively); between the two circulation states is the chaotic state, where thermal plumes erupt randomly and fail to be organized (see figure 4b). Figure 4(d) further shows the time segments of the dimensionless angular momentum $L(t)/L_0$ and the value of $L(t)/L_0$ of the three flow states shown in figure 4(a-c). It should be noted that the chaotic state in our study is different from the short transient state (i.e., the flow switching between the CLSC and CCLSC) in the 2D or quasi-2D square cells, as the duration time of the former is two or three orders of magnitude longer than that of the latter.

When the flow is in the circulation state, secondary rolls develop near the top and bottom circular walls. The formation of the secondary rolls is of the same origin as the corner rolls in the (quasi-)2D square cells: the interaction between the descending (ascending) side of the primary roll and the ascending (descending) plumes generated from the edge of the bottom (top) wall. Taking CCLSC as an example (see figure 4a), the descending side of the primary roll shears the ascending plumes from the left edge of the bottom wall, such that these plumes are forced to move horizontally to the right. Some of these plumes deflected down when they reach the right side of the wall and then follow the curved wall to the left, thus forming a small secondary roll at the bottom of the cell. Similarly, a secondary roll is formed at the top of the cell. These two secondary rolls are competing with the primary roll. When Ra is large, the primary roll becomes stronger, thus it can penetrate to very close to the top and bottom circular walls, and the secondary rolls would become smaller or even disappear. When Ra is small, the primary roll becomes weaker, it can not penetrate too much to very close to the top and bottom circular walls, thus the secondary roll would become bigger. This is indeed the case, as shown in figure
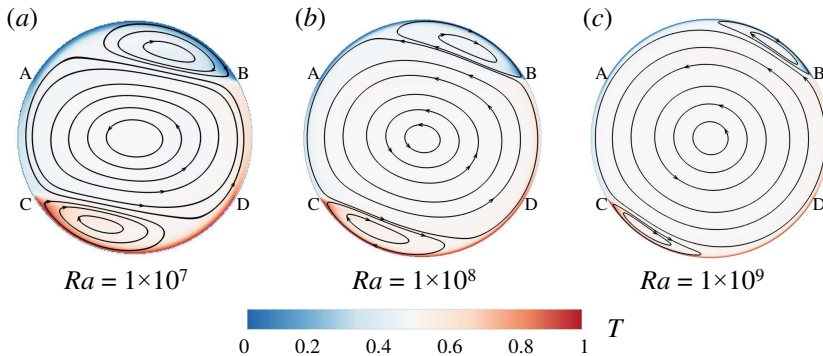
FIGURE 5. Time averaged temperature field (contour) and velocity field (arrows) of the flow for (a) $Ra = 1 \times 10^7$, (b) $Ra = 1 \times 10^8$, and (c) $Ra = 1 \times 10^9$, and $Pr = 4.3$. Arcs $\widehat{AB}$ and $\widehat{CD}$ denote the top and bottom one-third circular walls, respectively.

5(a-c), where the long time-averaged velocity field for $Ra = 1 \times 10^7$, 1×10^8 and 1×10^9, and $Pr = 4.3$ are given. We can see that with increasing Ra, the primary roll becomes larger, while the top and bottom secondary rolls become smaller. We would expect that at very high Ra, the secondary rolls will disappear, and a single roll structure occupies the whole cell. The above conjecture is supported by the experimentally observed single roll structure in the vertical circular thin disk at high Ra ($3 \times 10^9 \leqslant Ra \leqslant 2 \times 10^{10}$) where the secondary rolls are absent (Song *et al.* 2011, 2014; Wang *et al.* 2018*b,c*). In addition, previous studies (Xia *et al.* 2003; Zhou & Chen 2018) suggest that in the (quasi-)2D square cells, the corner rolls will also become smaller with increasing Ra. In our 2D simulations, we choose a smaller parameter space of Ra compared to those in experiments (Song *et al.* 2011, 2014; Wang *et al.* 2018*b,c*). The reason is that flow reversal starts to occur at smaller Ra in the 2D cell compared to those in the quasi-2D cell (Sugiyama *et al.* 2010).

We then measure the residence time, i.e., the percentage of time the flow spent in the two circulation states and the chaotic state, respectively. The criteria to quantitatively identify these flow states transitions are similar to those used in Huang & Xia (2016). First, the flow should stay at the current state for more than one large eddy turnover time $t_E = 4\pi/\langle|\omega_c(t)|\rangle$, where ω_c denotes the vorticity at the cell center. Secondly, the flow states should be clearly distinguished from each other, which is quantified by the three distinguishable peaks of the PDFs of $L(t)/L_0$. Thirdly, when the flow changes from one state to another, the value of $L(t)/L_0$ should be larger (or smaller) than the peak value in the PDF corresponding to the new flow state. We plot the residence time as a function of Ra for different Pr, as shown in figure 6. It is seen from the figure that for low Pr (e.g., $Pr = 2.0$ and $Pr = 3.0$), most of the time the flow is in the circulation states for the whole Ra range investigated (e.g., $10^7 \leqslant Ra \leqslant 10^8$). For intermediate Pr (e.g., $4.3 \leqslant Pr \leqslant 10.0$), the time the flow spent in the circulation state increases with Ra, while the time the flow spent in the chaotic state decreases, which implies that the flow is more organized at higher Ra. The fact that the circulation states are prevailing for higher Ra (at intermediate Pr) is consistent with the experimental results in the vertical circular thin disk (Wang *et al.* 2018*b*) where the chaotic state seems absent. For high Pr (e.g., $Pr = 15.0$ and 20.0), most of the time, the flow is in the chaotic state for the whole Ra range investigated. The Pr dependency of the flow state can be understood as follows: at low Pr, due to the large thermal diffusivity, very energetic vertical plumes which could
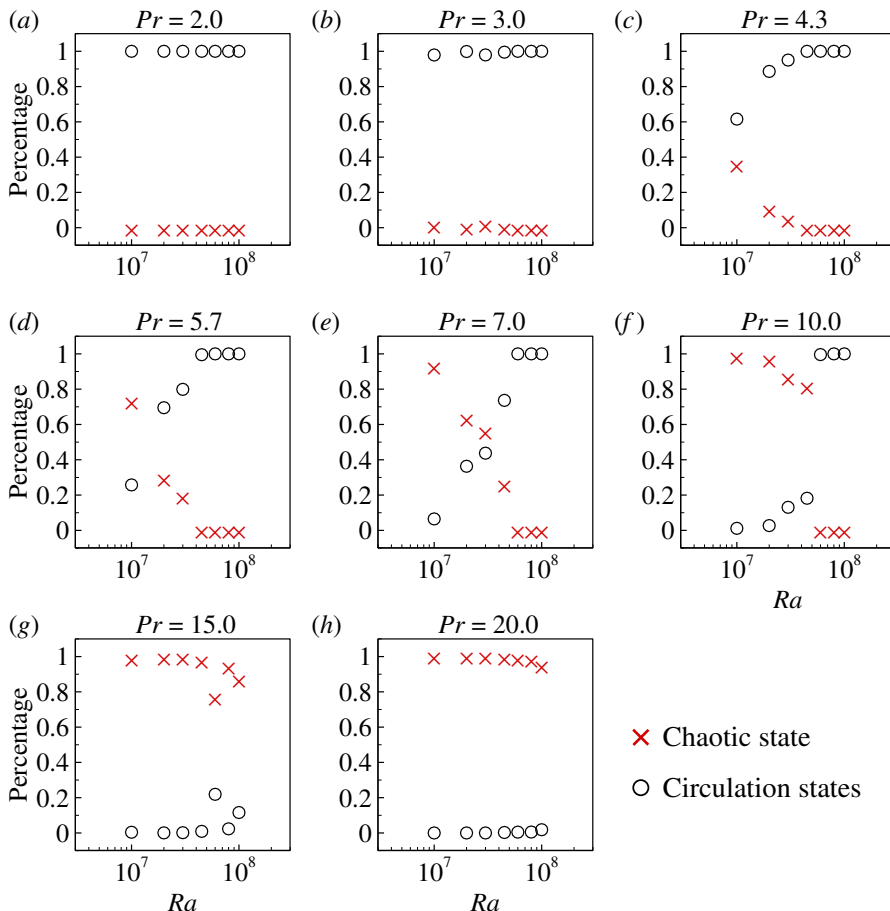
FIGURE 6. The residence time, i.e., percentage of time the flow spent in the two circulation states and the chaotic state for (*a*) *Pr* = 2.0, (*b*) *Pr* = 3.0, (*c*) *Pr* = 4.3, (*d*) *Pr* = 5.7, (*e*) *Pr* = 7.0, (*f*) *Pr* = 10.0, (*g*) *Pr* = 15.0, and (*h*) *Pr* = 20.0.

destroy the LSC are not likely to be formed, thus, the LSC remains stable; at higher *Pr*, due to the lower thermal diffusivity, the plumes are very likely to be energetic, they tend to ascend and descend vertically thus fail to organize into an LSC.

To understand how the flow switches from the circulation state to the chaotic state, we check the flow and temperature fields during the breakup of the primary roll, namely, the transition from one of the circulation states to the chaotic state. The breakup process of the primary roll in the circular cell is very similar to that in the 2D square cell, as shown in figure 7. Detached hot (or cold) plumes from the bottom (or top) circular walls are trapped in the secondary rolls, further feeding energy to the growth of the secondary flows (see figure 7b). With the growth of the secondary rolls in size, they gradually break the primary roll and connect to form a new primary roll (see figures 7c and 7d). However, the newly formed roll is unstable, it will be squeezed and further destructed by the growth of secondary rolls, thus the flow enters a chaotic state. The above stage is different from that in the 2D square cell, where a new LSC in the opposite direction will be organized shortly after the destruction of the old LSC, as discussed in detail in Section 3.3.

It was conjectured (Roche *et al.* 2002; Chilla *et al.* 2004) and shown by experiments (Sun *et al.* 2005; Xi & Xia 2008*b*; Weiss & Ahlers 2011*a,b*; Xi *et al.* 2016) as well as
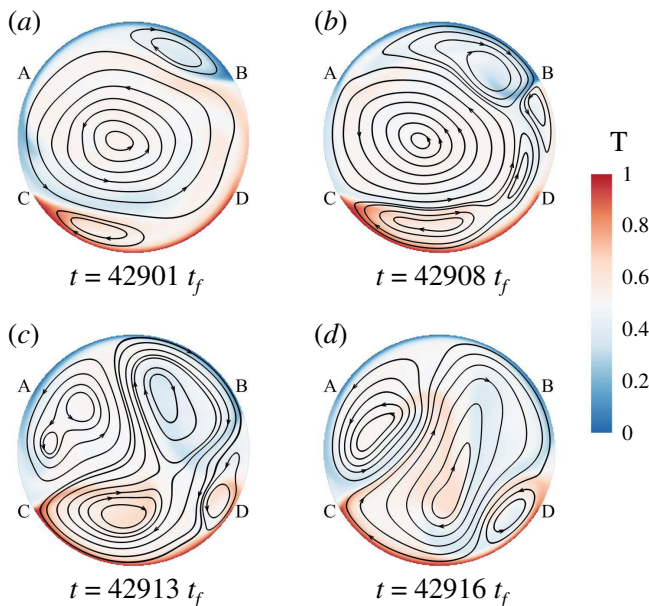
FIGURE 7. Typical snapshots of the flow field (temperature field and streamlines) during the breakup of the primary roll at (*a*) $t = 42901 \, t_f$, (*b*) $t = 42908 \, t_f$, (*c*) $t = 42913 \, t_f$, and (*d*) $t = 42916 \, t_f$. Arcs $\widehat{AB}$ and $\widehat{CD}$ denote the top and bottom one-third circular walls, respectively.

simulations (van der Poel *et al.* 2011, 2012) that the internal flow states are manifested by global quantities, such as the global heat transfer. To check whether it is the case in the 2D circular cells, we now examine the conditional averaged Nusselt and Reynolds numbers in the chaotic state and the circulation states. In figure 8, we plot their differences $Nu_{\mathrm{chao}}/Nu_{\mathrm{cir}} - 1$ and $Re_{\mathrm{chao}}/Re_{\mathrm{cir}} - 1$ as functions of Ra for various Pr. Here, the subscripts 'chao' and 'cir' denote the chaotic state and the circulation states, respectively. Because the chaotic state is absent (or almost absent) at $Pr = 2.0$ and 3.0, and the circulation states are absent (or almost absent) at $Pr = 15.0$ and 20.0, we only present results for $4.3 \leqslant Pr \leqslant 10.0$. From figure 8, we can see that for the chaotic state, the conditional averaged Nu is larger while the conditional averaged Re is smaller than those when the flow is in the circulation states. The less heat transfer efficiency in the circulation states is presumably due to that the primary roll separates the top and the bottom secondary rolls, the lack of direct communication between the top and the bottom walls results in the reduction of the heat transfer. While in the chaotic state, the plumes erupted from the top and bottom circular walls can travel directly to the opposite walls, thus building up short channels for the heat transfer, resulting in a higher Nu. The behavior the Re is following an opposite trend, overall Re is larger when the flow is in the circulation states, implying a stronger flow in this flow state as it is well organized.

3.3. *The onset of the large-scale circulation in circular and square cells*

To understand the origin of the chaotic flow state in the 2D circular cell, which was not observed in the 2D square cell (Sugiyama *et al.* 2010), we examine the onset process of the LSC in the circular and square cells, respectively. Because the behavior of the LSC onset is sensitive to initial conditions, in figure 9, we show four groups of different initial settings for the temperature profiles in the circular and the square cell: i) a uniform distribution of temperature $(T_{\mathrm{hot}} + T_{\mathrm{cold}})/2$ in bulk; ii) a uniform distribution of temperature T_{cold}
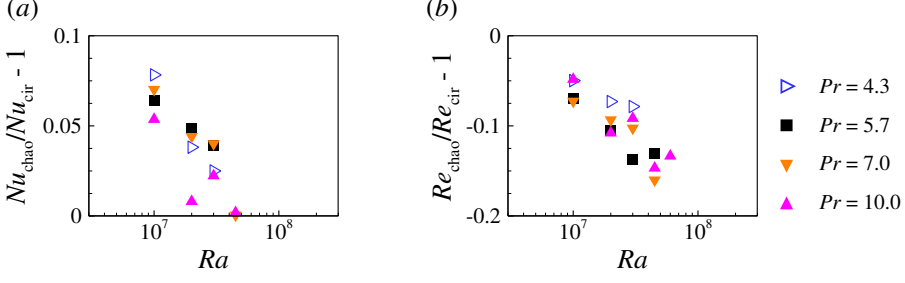
FIGURE 8. (a) $Nu_{\mathrm{chao}}/Nu_{\mathrm{cir}} - 1$ and (b) $Re_{\mathrm{chao}}/Re_{\mathrm{cir}} - 1$ as functions of Ra for various Pr. Here, Nu_{chao} and Nu_{cir} are the conditional averaged Nu when the flow is in the chaotic state and the circulation state, respectively. Re_{chao} and Re_{cir} are similarly defined.
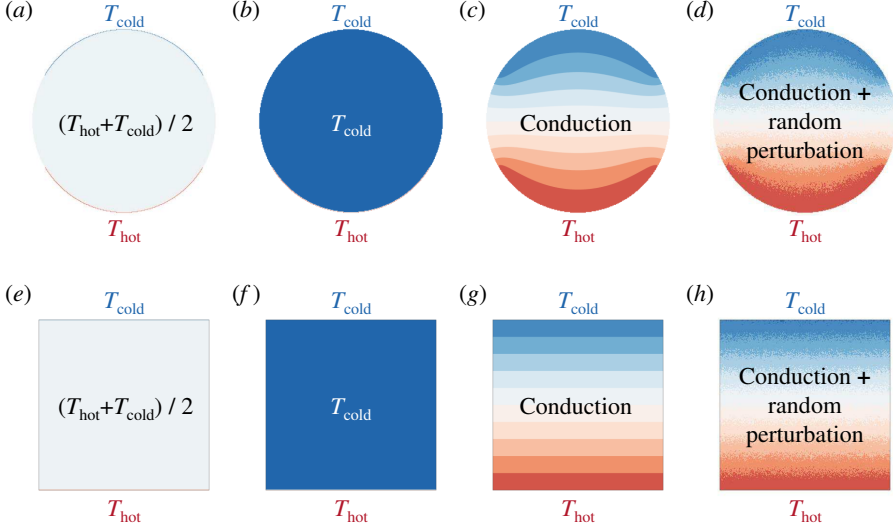

FIGURE 9. Different initial settings of the temperature profiles in (a-d) the circular cell and (e-h) the square cell. (a,e) a uniform distribution of temperature $(T_{\mathrm{hot}} + T_{\mathrm{cold}})/2$ in bulk; (b, f) a uniform distribution of temperature T_{cold} in bulk; (c,g) conduction temperature profile; (d,h) conduction temperature profile with random perturbation.

in bulk; iii) conduction temperature profile; iv) conduction temperature profile with random perturbation. Here, the conduction temperature profile was obtained via the steady temperature field at $Ra = 10^3$ and $Pr = 4.3$ (i.e., the Ra is below the threshold value for the onset of thermal convection). The random perturbation was achieved via superposing a uniformly distributed random number with a maximum/minimum value of $\pm 0.05 \cdot (T_{\mathrm{hot}} - T_{\mathrm{cold}})$ to the local temperature field.

In the following, we discuss in detail the onset of the LSC with the first group of initial temperature settings. For the other three groups of initial temperature settings, the onset processes exhibit similar even though not identical patterns. Figures 10 and 11 show the typical snapshots of temperature and velocity fields during the onset of the LSC in circular and square cells, respectively. The corresponding videos can be viewed in the supplementary movies 2 and 3. In the circular cell, starting from the time when the temperature difference is just applied to the top and bottom circular walls (referred to as quiescent state, see figure 9a), the thermal boundary layers develop near the top and
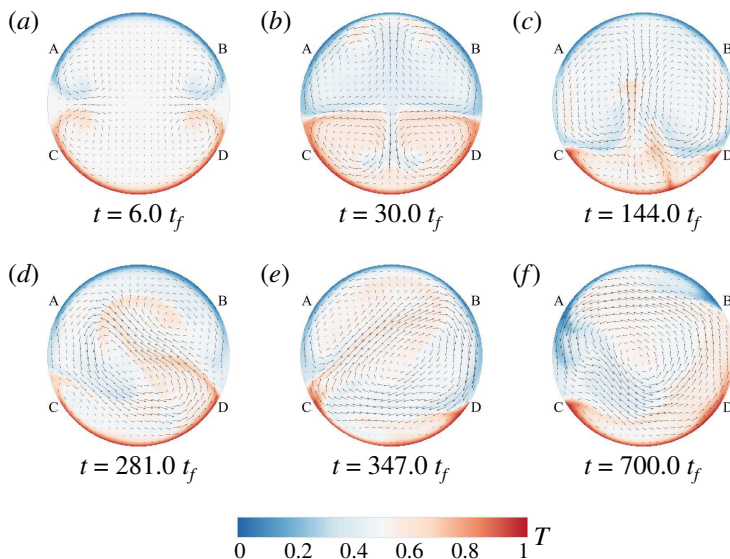
FIGURE 10. Snapshots of the flow fields (both the temperature contours and the velocity vectors) showing the onset of the large-scale circulation in the 2D circular cell at (*a*) $t = 6.0\ t_f$, (*b*) $t = 30.0\ t_f$, (*c*) $t = 144.0\ t_f$, (*d*) $t = 281.0\ t_f$, (*e*) $t = 347.0\ t_f$, (*f*) $t = 700.0\ t_f$ for $Ra = 10^7$ and $Pr = 4.3$. Initially, a uniform distribution of temperature $(T_{\text{hot}} + T_{\text{cold}})/2$ in bulk. It takes roughly $450\ t_f$ for the LSC to build up. Arcs $\overset{\frown}{AB}$ and $\overset{\frown}{CD}$ denote the top and bottom one-third circular walls, respectively.

bottom circular walls, the thermal plumes grow and detach from the edge of the boundary layers (marked as point A, B, C, and D in figure 10), where the temperature boundary conditions of the wall changes abruptly from constant temperature to adiabatic; the temperature field preserves both the top-bottom symmetry and left-right symmetry (see figure 10a). With the growing of plumes, the interactions between hot and cold plumes lead to the breakdown of top-down symmetry of the temperature field, while the left-right symmetry is still kept (see figure 10b). After that, the plumes start to have wavy-like motions, and the left-right symmetry of the temperature field is also broken. The plumes may also erupt from the centre of the boundary layers (see figure 10c). Then, the flow enters the chaotic state, where massive eruptions of the thermal plumes from either the left or the right edge of the boundary layer prevent the establishment of the LSC, and we can observe unstable clockwise or counterclockwise rotation roll in the cell centre (see figures 10d and 10e). The competition between the clockwise and counterclockwise rotation rolls continues until one of them wins, and a stable LSC is built-up (see figure 10f).

For comparison, we also study the onset of the LSC in the 2D square cell. In the square cell, starting from the quiescent state (see figure 9e), the thermal boundary layers develop near the top and bottom flat walls, thermal plumes detach from random locations on the boundary layers (see figures 11a-d). In the beginning, the flow is both up-down and left-right symmetric. When $t = 48.0\ t_f$, the up-down symmetry is broken. After the symmetry of the temperature field is broken, the plumes start to have wavy-like motions (see figure 11e). With more interactions among the plumes, the plumes start to organize spatially, where hot rising plumes move along the left sidewall and cold falling plumes move along the right sidewall (see figure 11f). The flow gradually evolved into a clockwise circulatory motion, and the LSC is formed. In the square cell, the symmetry of
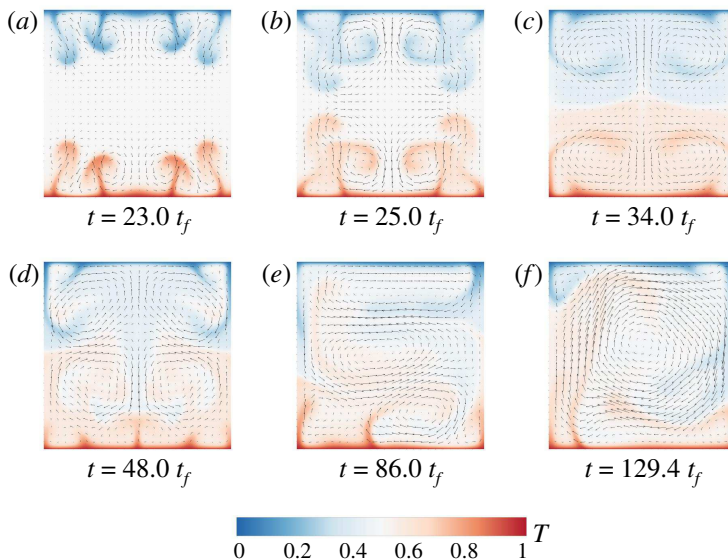
FIGURE 11. Snapshots of the flow fields (both the temperature contours and the velocity vectors) showing the onset of large-scale circulation in the 2D square cell at (a) $t = 23.0\, t_f$, (b) $t = 25.0\, t_f$, (c) $t = 34.0\, t_f$, (d) $t = 48.0\, t_f$, (e) $t = 86.0\, t_f$, (f) $t = 129.4\, t_f$ for $Ra = 10^7$ and $Pr = 4.3$. Initially, a uniform distribution of temperature $(T_{\mathrm{hot}} + T_{\mathrm{cold}})/2$ in bulk. It takes roughly 130 t_f for the LSC to build up.

the temperature field is easier to be broken compared to that in the circular cell. Once the symmetry of the temperature field is broken, the LSC will be quickly organized. It should be noted that the initial transient stage described here is different from that of experimental investigation (Xi *et al.* 2004), where the heating and cooling capacities for the bottom and top walls are not identical, thus the top-down boundary conditions are slightly asymmetric.

To further compare the organization of thermal plumes into the LSC in the 2D circular and square cells, we plot the dimensionless global angular momentum $L(t)/L_0$ during the onset process of the LSC, as shown in figure 12. For all the four cases, in the circular cell, L/L_0 fluctuates around zero, and it takes a while (around $t \gtrsim 500\, t_f$ in the first three cases and $t \gtrsim 100\, t_f$ in the last case) to reach a plateau well above zero, and the LSC is organized. In contrast, in the square cell, L/L_0 reaches a plateau well below (or above) zero with negative (or positive) fluctuations much earlier than that in the square cell (around $t \gtrsim 200\, t_f$ in the first three cases and $t \gtrsim 20\, t_f$ in the last case), indicating the LSC in the clockwise (or counter-clockwise) direction is organized. Specifically, in the circular cell, the plumes detach mainly from the edge of the top and bottom circular walls (marked as point A, B, C, and D in figure 10). In contrast, in the square cell, the plumes detach from random horizontal positions on the top and bottom circular walls (see figure 11), there is no competition between rolls rotated in opposite directions. Thus, in the 2D circular cell, it takes a longer time to establish a stable LSC, and the obstruction to building the stable LSC may further result in the chaotic flow state.

3.4. *Flow mode decomposition and modes evolution during a reversal*

Since high-order flow modes play important roles in the dynamical process of the reversal of the LSC (Mishra *et al.* 2011; Xi *et al.* 2016), we perform Fourier mode decomposition to the velocity field, which is convenient to operate and has been employed to study
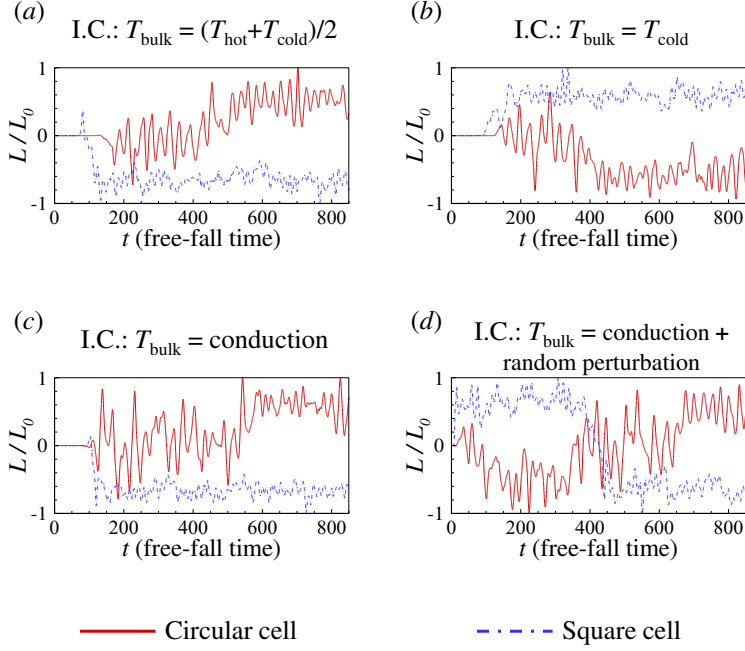
FIGURE 12. The time trace of the dimensionless global angular momentum $L(t)/L_0$ in the 2D circular and square cell with $Ra = 10^7$ and $Pr = 4.3$, showing the onset of large-scale circulation, for different initial settings: (a) a uniform distribution of temperature $(T_{hot} + T_{cold})/2$ in bulk; (b) a uniform distribution of temperature T_{cold} in bulk; (c) conduction temperature profile; (d) conduction temperature profile with random perturbation.

flow reversal mechanisms in 2D and quasi-2D square convection cells (Petschel *et al.* 2011; Chandra & Verma 2011, 2013; Wang *et al.* 2018a; Chen *et al.* 2019). Specifically, the instantaneous velocity field (u, v) is projected onto the Fourier basis $(\hat{u}^{m,n}, \hat{v}^{m,n})$ as

$$u(x, y, t) = \sum_{m,n} A_x^{m,n}(t)\hat{u}^{m,n}(x, y) \tag{3.1}$$

$$v(x, y, t) = \sum_{m,n} A_y^{m,n}(t)\hat{v}^{m,n}(x, y) \tag{3.2}$$

Here, the Fourier basis $(\hat{u}^{m,n}, \hat{v}^{m,n})$ is chosen as

$$\hat{u}^{m,n}(x, y) = 2\sin(m\pi x)\cos(n\pi y) \tag{3.3}$$

$$\hat{v}^{m,n}(x, y) = -2\cos(m\pi x)\sin(n\pi y) \tag{3.4}$$

the instantaneous amplitude of the Fourier mode is then calculated as

$$A_x^{m,n}(t) = \langle u(x, y, t), \hat{u}^{m,n}(x, y) \rangle = \sum_i \sum_j u(x_i, y_i, t)\hat{u}^{m,n}(x_i, y_i) \tag{3.5}$$

$$A_y^{m,n}(t) = \langle v(x, y, t), \hat{v}^{m,n}(x, y) \rangle = \sum_i \sum_j v(x_i, y_i, t)\hat{v}^{m,n}(x_i, y_i) \tag{3.6}$$

where $\langle u, \hat{u} \rangle$ and $\langle v, \hat{v} \rangle$ denote the inner product of u and $\hat{u}$, v and $\hat{v}$, respectively. The above Fourier mode decomposition approach was originally designed to study flow behaviours in a square domain. To extend this approach in the circular cell, we still
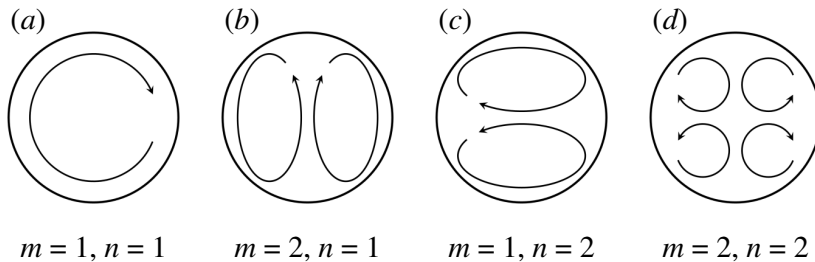
FIGURE 13. Schematic illustrations of the first four Fourier modes.

choose the square domain for computing the Fourier basis but set the velocity vectors that fall outside the circular to be zero. It should be noted that the Fourier basis described by Eqs. (3.3) and (3.4) may not be very accurate for a circular cell, since they are originally designed for a square cell. However as the Fourier basis mainly capture flows in the bulk region, and the cell corners have minor effects on the Fourier mode analysis (Chen *et al.* 2020), the Fourier basis used here indeed captured the main structure of the bulk flow. Actually, even in the square cell, the Fourier basis functions do not satisfy the no-slip boundary condition, yet they capture the convective flow profile well (Chandra & Verma 2011). The energy in each Fourier mode is calculated as $E^{m,n}(t) = \sqrt{[A_x^{m,n}(t)]^2 + [A_y^{m,n}(t)]^2}$. The (m, n) Fourier mode corresponds to a flow structure with m rolls in the x-direction and n rolls in the y-direction, as illustrated in figure 13. In the following, we will consider m and $n = 1, 2, 3$, namely the first nine Fourier modes.

The time evolution of energy contained in each Fourier mode during a flow reversal from $t = 42\ 500\ t_f$ to $43\ 500\ t_f$ (the same data set as in figure 4d) is plotted in figure 14. Here, we normalize energy of the (m, n) mode $E^{m,n}$ by the total energy $E_{total}(t) = \sum E^{m,n}(t)$. According to the time segments of the dimensionless angular momentum shown in figure 4(d), the flow is in the stable LSC during $42\ 500\ t_f \leqslant t \leqslant 42\ 900\ t_f$ and $43\ 100\ t_f \leqslant t \leqslant 43\ 500\ t_f$. We can see from figure 14, during this period, the dominant Fourier modes are the $(1, 1)$ and $(1, 3)$ modes since they account for over 20% of the total energy. The prevailing of the $(1, 1)$ and the $(1, 3)$ modes are consistent with the fact that the flow is in the shape of a primary roll in the middle, as well as secondary rolls near the top and bottom circular walls. Between the two successive circulation states, the energy of the $(2, 1)$, $(1, 2)$, $(2, 2)$, and $(2, 3)$ modes grow, and these higher-order flow modes might correspond to the massive plumes eruptions in the chaotic state.

To check the validation of the above described Fourier mode decomposition approach on the circular cell, we perform proper orthogonal decomposition (POD) of the flow during a reversal, which does not require prior knowledge of the geometry of the flow domain (Berkooz *et al.* 1993). The POD analysis has been employed to study flow reversal mechanisms in both 2D and 3D convection cells (Podvin & Sergent 2015, 2017; Castillo-Castellanos *et al.* 2019; Soucasse *et al.* 2019). Specifically, the flow variables $\mathbf{U}(\mathbf{x}, t)$ is decomposed as a superposition of empirical orthogonal eigenfunctions $\phi_i(\mathbf{x})$ and their amplitudes $a_i(t)$ as

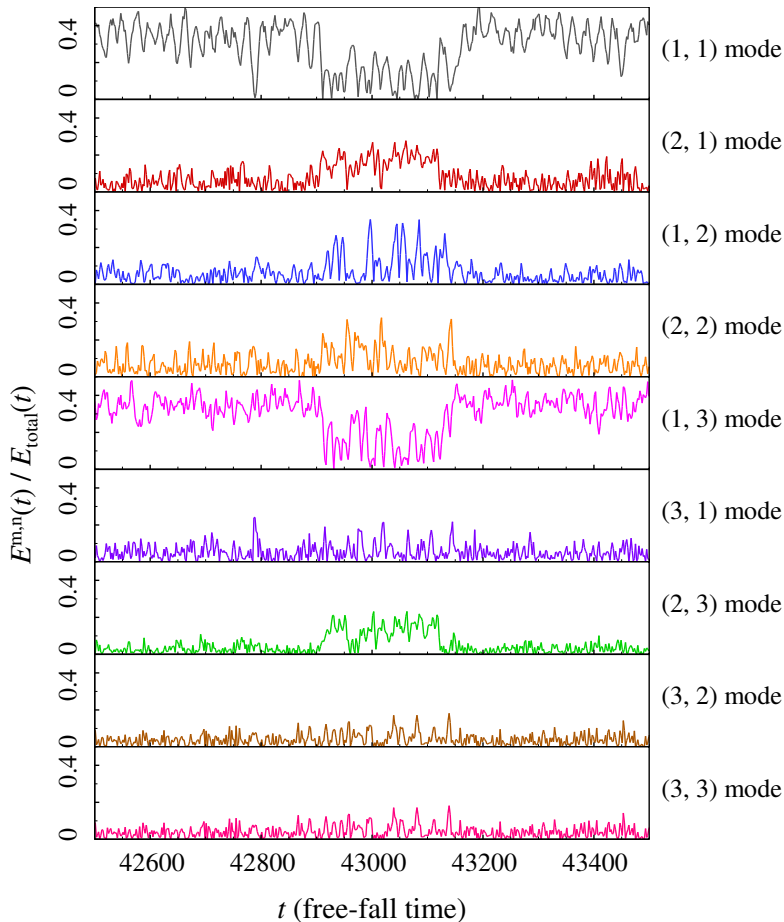$$\mathbf{U}(\mathbf{x}, t) = \sum_{i=1}^{\infty} a_i(t)\phi_i(\mathbf{x}) \tag{3.7}$$

FIGURE 14. Time evolution of the energy contained in the first nine Fourier modes during one reversal of the LSC for $Ra = 10^7$ and $Pr = 4.3$.

The eigenfunctions $\phi_i(\mathbf{x})$ are solutions of the eigenvalue problem

$$\int_{\Omega} \left[\frac{1}{N} \sum_{k=1}^{N} \mathbf{U}(\mathbf{x}, t_k) \mathbf{U}(\mathbf{x}', t_k) \right] \phi_i(\mathbf{x}') d\mathbf{x}' = \lambda_i \phi_i(\mathbf{x}) \qquad (3.8)$$

where Ω is the spatial domain, and N is the number of total snapshots. If the empirical eigenfunctions are normalized, we have $\langle a_i(t) a_j(t) \rangle_t = \delta_{ij} \lambda_i$, where δ_{ij} is Kroneker symbol and λ_i is the energy of the ith POD mode. Figure 15 $(a\text{-}e)$ shows the first five most energetic POD modes, which were obtained on a dataset of 40 000 snapshots spanning 10 000 $t_f \leqslant t \leqslant 50\ 000\ t_f$ for $Ra = 10^7$ and $Pr = 4.3$. From the energy contained in each mode (shown in figure 15f), we can see that the first mode accounts for over 60% of the total energy, while each of the other higher-order modes accounts for less than 10% of the total energy. The most energetic POD mode consists of a primary roll in the cell centre and two secondary rolls near the top and bottom circular walls, which is similar to the mean-field shown in figure 5. The superposition of the second and the fifth most energetic POD modes are associated with a quadrupole flow, which corresponds to the (2, 2) Fourier mode. The superposition of the third and the forth most energetic POD mode consists of two big rolls superposed in the vertical direction, and it corresponds to
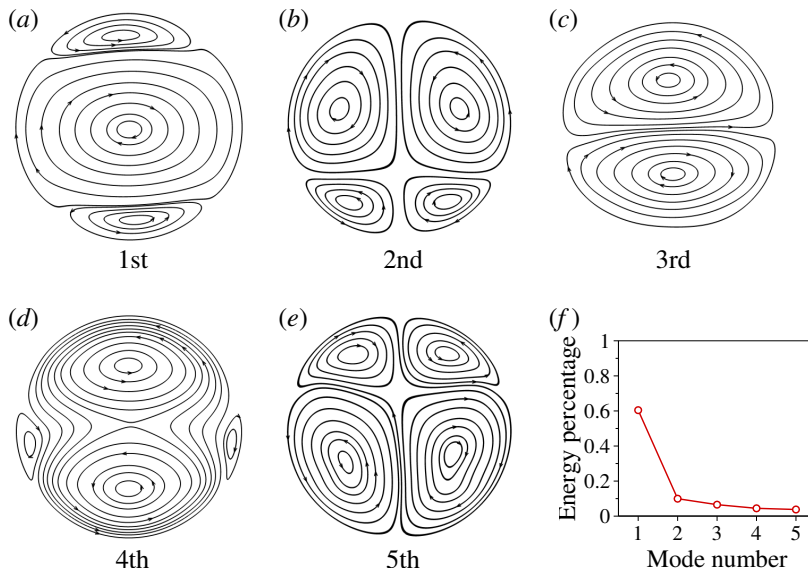
FIGURE 15. (*a-e*) The first five most energetic POD modes and (*f*) the energy contained in each mode, for $Ra = 10^7$ and $Pr = 4.3$.

Fourier mode	(1, 1) + (1, 3)	(2, 2)	(1, 2)
(Energy percentage)	55.5%	8.1%	7.3%
POD mode	1st	2nd + 5th	3rd + 4th
(Energy percentage)	60.4%	13.8%	11.0%

TABLE 2. Comparison of the energy contained in the Fourier modes and the POD modes.

the (1, 2) Fourier mode. In addition, we compare the energy contained in the POD modes and the Fourier modes for the same flow dataset, as shown in table 2. We can see that the energies contained in the first five POD modes are consistent with those in (1, 1) + (1, 3), (2, 2), and (1, 2) Fourier mode, respectively. Thus, the one-to-one correspondence between the POD mode and the Fourier mode suggests the validity of the Fourier mode decomposition in the circular cell. In the following, we will focus on the Fourier mode decomposition to analyze the high-order flow modes, in which the same basis functions can be adopted for different Ra and Pr flows (in contrast to POD analysis, where the rankings of the first several major flow modes might be different for different Ra and Pr).

To study the relationship between different Fourier modes, we calculate the cross-correlation function between the energy contained in the (1, 1) mode and the other higher-order modes as

$$R_{E^{1,1},E^{m,n}}(\tau) = \frac{\langle [E^{1,1}(t+\tau) - \langle E^{1,1}\rangle][E^{m,n}(t) - \langle E^{m,n}\rangle]\rangle}{\sigma_{E^{1,1}}\sigma_{E^{m,n}}}, \qquad (3.9)$$

where $\sigma_{E^{m,n}}$ is the standard deviation of the energy of the (m, n) mode $E^{m,n}$. As shown in figure 16(a), $R_{E^{1,1},E^{1,3}}$ show positive peak near $\tau/t_E = 0$, implying that the strength of the (1, 1) and (1, 3) flow modes are positively correlated; meanwhile, the strength of other higher-order modes are negatively correlated with $E^{1,1}$. The results from this statistical
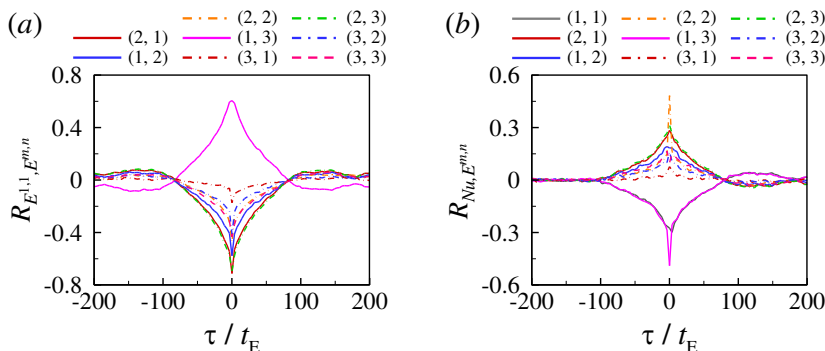
FIGURE 16. Cross-correlation functions (*a*) between $E^{1,1}$ and $E^{m,n}$, (*b*) between the instantaneous Nu and $E^{m,n}$, as a function of lag time τ/t_E for $Ra = 10^7$ and $Pr = 4.3$.

analysis are consistent with that we have learned from the instantaneous example (see figure 14): when the (1, 1) mode becomes weaker, the (1, 3) mode also becomes weaker, and *vice versa*. It is also noted that the correlation between the (1, 1) mode and the (2, 2), (2, 3), and (2, 1) modes all have negative peaks near $\tau/t_E = 0$, indicating these higher-order modes themselves are positively correlated. In addition, we study the relationship between the heat transfer efficiency and the energy contained in different modes by calculating their cross-correlation functions as

$$R_{Nu,E^{m,n}}(\tau) = \frac{\langle [Nu(t+\tau) - \langle Nu \rangle][E^{m,n}(t) - \langle E^{m,n} \rangle] \rangle}{\sigma_{Nu}\sigma_{E^{m,n}}}, \qquad (3.10)$$

where σ_{Nu} and $\sigma_{E^{m,n}}$ are the standard deviation of Nu and the energy of the (m,n) mode $E^{m,n}$, respectively. As shown in figure 16(b), Nu is negatively correlated with $E^{1,1}$ and $E^{1,3}$, which means that the (1, 1) and (1, 3) flow modes are associated with smaller heat transfer efficiency on average; meanwhile, the other higher-order modes, including the (2, 2), (2, 3) and (2, 1) modes, are positively correlated with Nu. These results are consistent with results from the conditional averaged Nusselt number shown in figure 8(a), *i.e.*, the Nu is smaller when the flow is in the circulation states (corresponding to the (1, 1) and (1, 3) flow modes).

We further calculate the time-averaged energies contained in each Fourier mode $\langle E^{m,n} \rangle$ as a function of Ra for various Pr, and normalize the values with the time-averaged total energies $\langle E_{total} \rangle$. From figure 17 we can see that, at lower Pr (e.g., $Pr = 2.0$ and $Pr = 3.0$), the (1, 1) and (1, 3) modes are dominated and they together contain more than 70% of the total flow energy, resulting in a stable LSC and no (or rare) flow reversal events. At higher Pr (e.g., $Pr = 20.0$), both the (1, 1) and (1, 3) modes are very weak, thus the stable LSC does not exist. At intermediate Pr, the (1, 1) and (1, 3) modes are weaker at lower Ra, thus the LSC can be easily broken, further leads to its reversal; with increasing Ra, the (1, 1) and (1, 3) modes become stronger, implying that the LSC is stable. We also note the Ra and Pr dependencies of the time-averaged energies are similar to those of the residence time shown in figure 6, mainly because the (1, 1) and (1, 3) modes are dominant in the circulation states.

3.5. *Phase diagram of the flow states and reversal in Ra-Pr plane*

With long-time simulations in a wide range of Ra and Pr parameter spaces, we can then obtain the phase diagram of whether the flow is in the form of an LSC and whether the reversal of the LSC could occur, as shown in figure 18. The criteria to detect whether
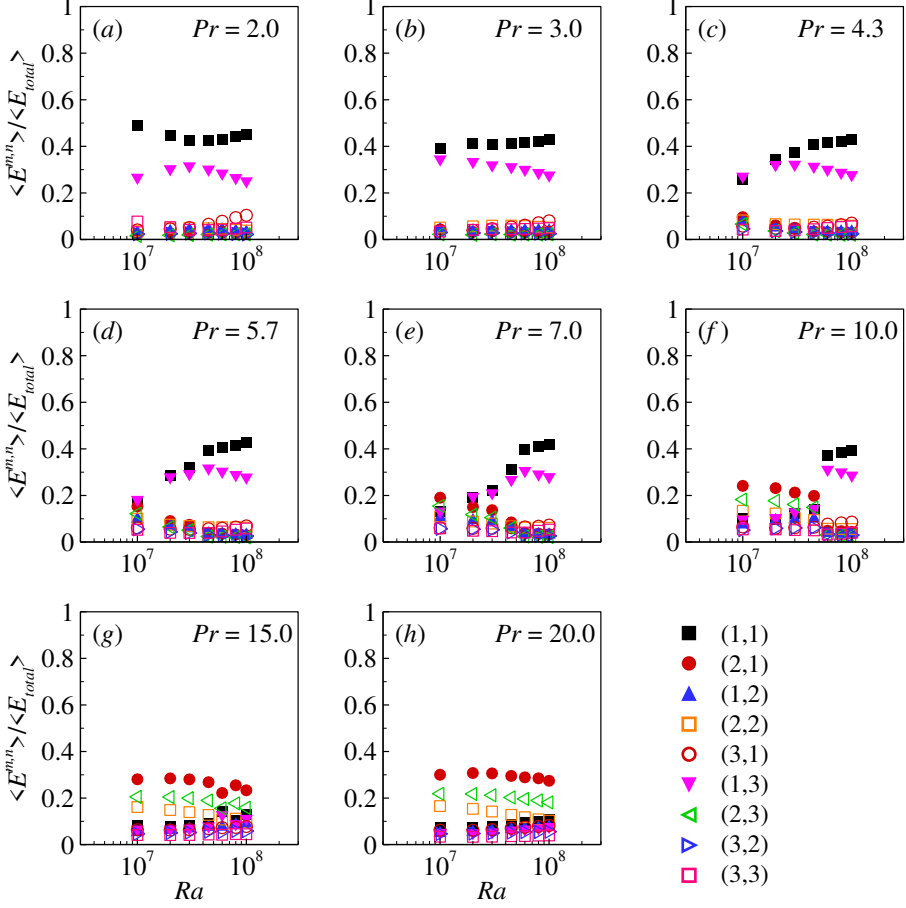
FIGURE 17. Time-averaged energy contained in each of the first nine Fourier modes as functions of Ra for (a) $Pr = 2.0$, (b) $Pr = 3.0$, (c) $Pr = 4.3$, (d) $Pr = 5.7$, (e) $Pr = 7.0$, (f) $Pr = 10.0$, (g) $Pr = 15.0$, and (h) $Pr = 20.0$.

an LSC exists is based on checking the value of dimensionless angular momentum. If L/L_0 reaches a plateau well above (below) zero with positive (negative) fluctuations, it corresponds to an LSC organized in counterclockwise (clockwise) direction. The criteria to detect whether the LSC reversals occur has been described in Section 3.2. The phase diagram in the $Ra - Pr$ plane can be understood in terms of competition between the thermal and viscous diffusions. For high Pr or low Ra (corresponding to the top-left region of the phase diagram in figure 18a), the flow is in the chaotic state, and the LSC is not formed, let alone the reversal of the LSC; for low Pr or high Ra, the flow is in the circulation states, and there is only stable LSC (see the bottom-right region of the phase diagram in figure 18b). From figure 18b, we can see that the LSC reversal only occurs at a limited Ra and Pr range. We note that the phase diagram shown here is very similar to that for 2D/quasi-2D square cell in Sugiyama *et al.* (2010) where the phase diagram is understood based on the growth of the corner rolls. And the reason that there is no reversal occurring for very small Pr or very high Pr is that in those cases the building up of the corner rolls are suppressed. As in the circular cell the LSC is still not a single roll but with two secondary rolls, the reversal must be understood in terms of the interaction between the main roll and the corner rolls. Thus the argument used in Sugiyama *et al.*
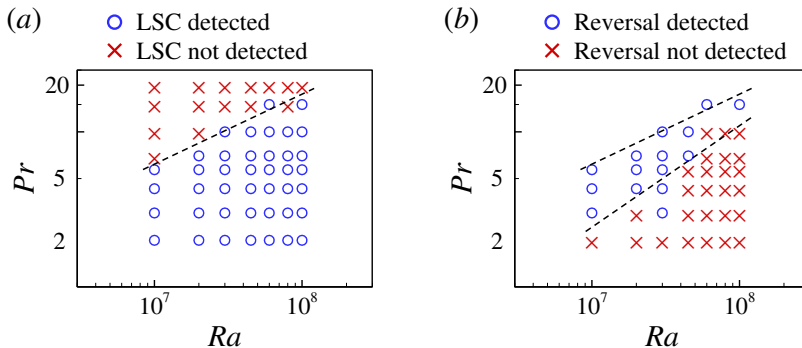
FIGURE 18. Phase diagram of (*a*) the flow states and (*b*) the flow reversals in the *Ra-Pr* plane. The gray dashed lines represent the estimated boundaries between the different states. The upper boundary in (*b*) is the same as the boundary in (*a*).

(2010) for the 2D/quasi-2D square cell could be directly borrowed to understand the reversals in the circular cell, at least in the parameter range of the current study. The flow in the circular cell will probably evolve into a single roll without the secondary rolls when *Ra* becomes very large. In that regime, the reversal then should be understood solely in terms of the dynamics of the single roll itself.

4. Conclusions

In this work, we have performed long-time direct numerical simulations of turbulent thermal convection in 2D circular cells. We observed three meta-stable flow states exist in the convection of 2D circular cell, namely, the two circulation states (both clockwise and counterclockwise), and the chaotic state characterized with incoherent plumes motions. The chaotic state is a manifestation of the fact that it is difficult for the plumes to organize into the coherent LSC. We found that the chaotic state dominant the flow for high *Pr*, while the circulations state dominant the flow for low *Pr*. For the intermediate *Pr*, the circulation states become stronger while the chaotic state becomes weaker, with increasing *Ra*. We also found that the internal flow states manifested themselves into the global properties such as Nusselt number and Reynolds number: the *Nu* number is up to 8% larger in the chaotic state than that in the circulation states, and the *Re* is up to 17% smaller in the chaotic state than that in the circulation states. Intuitively one would imagine that more coherent and stronger flow will have higher heat transfer efficiency, while the results shown here, i.e., the stronger and more coherent circulation state inducing lower *Nu*, is counter-intuitive and awaiting further study.

The original objective of adopting the circular cell was to make the geometry of the cell to perfectly fit the circulatory flow, i.e., the LSC, and get rid of the corner rolls and their effects on the dynamics such as the reversal of the LSC. While it is found that in the circular cell it is not the case that one single LSC occupies the while cell, at least in the parameter range of the current study, instead the circulation states of the flow consist of one primary roll in the middle and two secondary rolls near the top and bottom circular walls. The top and bottom secondary rolls in the circular cell and the two corner rolls in the square cell are from the same origin, namely, the interaction between the mean flow and the plumes erupted from edges (corners) of the top and bottom circular walls. The primary roll becomes stronger and larger, while the two secondary rolls become weaker and smaller, with increasing *Ra*. When the flow transits from the circulation state to the chaotic state, the secondary rolls played important roles. They grow in size and energy,

squeeze and finally break up the primary roll. The reversal of the LSC is accompanied by the growth of top and bottom secondary rolls, the breaking of the primary roll, and the connection of the secondary rolls.

Finally, we mapped out the phase diagram of whether the flow is organized as an LSC and whether the reversal could occur. In the range of $10^7 \leqslant Ra \leqslant 10^8$ and $2.0 \leqslant Pr \leqslant 20.0$, it is found the flow is in an organized LSC when Ra is large and Pr is small. The reversal of the LSC could only occur in a limited Pr and Ra range. As in the parameter range of the current study, the circulation state of the flow consists of the main roll and the secondary rolls, the reversal of the LSC should not be understood solely in terms of the dynamics of the main roll itself, but a combined effect of the interaction between the main roll and the secondary rolls, and the stability of the main roll itself.

5. Acknowledgments

6. Declaration of interests

The authors report no conflict of interest.

7. Supplementary movies

Supplementary movies are available at https://doi.org/10.1017/jfm.xxxxxx.

REFERENCES

AHLERS, G., GROSSMANN, S. & LOHSE, D. 2009 Heat transfer and large scale dynamics in turbulent Rayleigh-Bénard convection. *Rev. Mod. Phys.* **81** (2), 503.

AIDUN, C. K. & CLAUSEN, J. R. 2010 Lattice-Boltzmann method for complex flows. *Annu. Rev. Fluid Mech.* **42**, 439–472.

BERKOOZ, G., HOLMES, P. & LUMLEY, J. L. 1993 The proper orthogonal decomposition in the analysis of turbulent flows. *Annu. Rev. Fluid Mech.* **25** (1), 539–575.

BIGGIN, A. J., STEINBERGER, B., AUBERT, J., SUTTIE, N., HOLME, R., TORSVIK, T. H., VAN DER MEER, D. G. & VAN HINSBERGEN, D.J.J. 2012 Possible links between long-term geomagnetic variations and whole-mantle convection processes. *Nature Geosci.* **5** (8), 526–533.

BOUZIDI, M., FIRDAOUSS, M. & LALLEMAND, P. 2001 Momentum transfer of a Boltzmann-lattice fluid with boundaries. *Phys. Fluids* **13** (11), 3452–3459.

BROWN, E. & AHLERS, G. 2006 Rotations and cessations of the large-scale circulation in turbulent Rayleigh–Bénard convection. *J. Fluid Mech.* **568**, 351–386.

BROWN, E., NIKOLAENKO, A. & AHLERS, G. 2005 Reorientation of the large-scale circulation in turbulent Rayleigh-Bénard convection. *Phys. Rev. Lett.* **95** (8), 084503.

CASTILLO-CASTELLANOS, A., SERGENT, A., PODVIN, B. & ROSSI, M. 2019 Cessation and reversals of large-scale structures in square Rayleigh–Bénard cells. *J. Fluid Mech.* **877**, 922–954.

CASTILLO-CASTELLANOS, A., SERGENT, A. & ROSSI, M. 2016 Reversal cycle in square Rayleigh–Bénard cells in turbulent regime. *J. Fluid Mech.* **808**, 614–640.

CHANDRA, M. & VERMA, M. K. 2011 Dynamics and symmetries of flow reversals in turbulent convection. *Phys. Rev. E* **83** (6), 067303.

CHANDRA, M. & VERMA, M. K. 2013 Flow reversals in turbulent convection via vortex reconnections. *Phys. Rev. Lett.* **110** (11), 114503.

CHEN, S. & DOOLEN, G. D. 1998 Lattice Boltzmann method for fluid flows. *Annu. Rev. Fluid Mech.* **30** (1), 329–364.

CHEN, X., HUANG, S.-D., XIA, K.-Q. & XI, H.-D. 2019 Emergence of substructures inside the large-scale circulation induces transition in flow reversals in turbulent thermal convection. *J. Fluid Mech.* **877**, R1.

CHEN, X., WANG, D.-P. & XI, H.-D. 2020 Reduced flow reversals in the absence of corner vortices. *J. Fluid Mech.* **891**, R5.

CHILLA, F., RASTELLO, M., CHAUMAT, S. & CASTAING, B. 2004 Long relaxation times and tilt sensitivity in Rayleigh-Bénard turbulence. *Eur. Phys. J. B* **40** (2), 223–227.

CHILLÀ, F. & SCHUMACHER, J. 2012 New perspectives in turbulent Rayleigh-Bénard convection. *Eur. Phys. J. E* **35** (7), 58.

CILIBERTO, S., CIONI, S. & LAROCHE, C. 1996 Large-scale flow properties of turbulent thermal convection. *Phys. Rev. E* **54** (6), R5901.

CIONI, S., CILIBERTO, S. & SOMMERIA, J. 1997 Strongly turbulent Rayleigh–Bénard convection in mercury: comparison with results at moderate Prandtl number. *J. Fluid Mech.* **335**, 111–140.

VAN DOORN, E., DHRUVA, B., SREENIVASAN, K. R. & CASSELLA, V. 2000 Statistics of wind direction and its increments. *Phys. Fluids* **12** (6), 1529–1534.

FUNFSCHILLING, D. & AHLERS, G. 2004 Plume motion and large-scale circulation in a cylindrical Rayleigh-Bénard cell. *Phys. Rev. Lett.* **92** (19), 194502.

GALLET, B., HERAULT, J., LAROCHE, C., PÉTRÉLIS, F. & FAUVE, S. 2012 Reversals of a large-scale field generated over a turbulent background. *Geophys. Astrophys. Fluid Dyn.* **106** (4-5), 468–492.

GLATZMAIER, G. A., COE, R. S., HONGRE, L. & ROBERTS, P. H. 1999 The role of the Earth's mantle in controlling the frequency of geomagnetic reversals. *Nature* **401** (6756), 885–890.

HUANG, S.-D. & XIA, K.-Q. 2016 Effects of geometric confinement in quasi-2-D turbulent Rayleigh–Bénard convection. *J. Fluid Mech.* **794**, 639–654.

KACZOROWSKI, M. & XIA, K.-Q. 2013 Turbulent flow in the bulk of Rayleigh–Bénard convection: small-scale properties in a cubic cel. *J. Fluid Mech.* **722**, 596–617.

KERR, R.M. 1996 Rayleigh number scaling in numerical convection. *J. Fluid Mech.* **310**, 139–179.

KRISHNAMURTI, R. & HOWARD, L. N. 1981 Large-scale flow generation in turbulent convection. *Proc. Natl Acad. Sci. USA* **78** (4).

LI, L., MEI, R. & KLAUSNER, J. F. 2013 Boundary conditions for thermal lattice Boltzmann equation method. *J. Comput. Phys.* **237**, 366–395.

LOHSE, D. & XIA, K.-Q. 2010 Small-scale properties of turbulent Rayleigh-Bénard convection. *Annu. Rev. Fluid Mech.* **42**.

MIESCH, M. S. & TOOMRE, J. 2009 Turbulence, magnetism, and shear in stellar interiors. *Annu. Rev. Fluid Mech.* **41**, 317–345.

MISHRA, P. K., DE, A. K., VERMA, M. K. & ESWARAN, V. 2011 Dynamics of reorientations and reversals of large-scale flow in Rayleigh–Bénard convection. *J. Fluid Mech.* **668**, 480–499.

NI, R., HUANG, S.-D. & XIA, K.-Q. 2015 Reversals of the large-scale circulation in quasi-2D Rayleigh–Bénard convection. *J. Fluid Mech.* **778**.

PÉTRÉLIS, F., FAUVE, S., DORMY, E. & VALET, J.-P. 2009 Simple mechanism for reversals of Earth's magnetic field. *Phys. Rev. Lett.* **102** (14), 144503.

PETSCHEL, K., WILCZEK, M., BREUER, M., FRIEDRICH, R. & HANSEN, U. 2011 Statistical analysis of global wind dynamics in vigorous Rayleigh-Bénard convection. *Phys. Rev. E* **84** (2), 026309.

PODVIN, B. & SERGENT, A. 2015 A large-scale investigation of wind reversal in a square Rayleigh–Bénard cell. *J. Fluid Mech.* **766**, 172–201.

PODVIN, B. & SERGENT, A. 2017 Precursor for wind reversal in a square Rayleigh-Bénard cell. *Phys. Rev. E* **95** (1), 013112.

VAN DER POEL, E. P., STEVENS, R. J.A.M. & LOHSE, D. 2011 Connecting flow structures and heat flux in turbulent Rayleigh-Bénard convection. *Phys. Rev. E* **84** (4), 045303.

VAN DER POEL, E. P., STEVENS, R. JAM & LOHSE, D. 2013 Comparison between two-and three-dimensional Rayleigh–Bénard convection. *J. Fluid Mech.* **736**, 177–194.

VAN DER POEL, E. P., STEVENS, R. J.A.M., SUGIYAMA, K. & LOHSE, D. 2012 Flow states in two-dimensional Rayleigh-Bénard convection as a function of aspect-ratio and Rayleigh number. *Phys. Fluids* **24** (8), 085104.

ROCHE, P.-E., CASTAING, B., CHABAUD, B. & HÉBRAL, B. 2002 Prandtl and Rayleigh numbers dependences in Rayleigh-Bénard convection. *Europhys. Lett.* **58** (5), 693.

SHRAIMAN, B. I. & SIGGIA, E. D. 1990 Heat transport in high-Rayleigh-number convection. *Phys. Rev. A* **42** (6), 3650.

SILANO, G., SREENIVASAN, K.R. & VERZICCO, R. 2010 Numerical simulations of Rayleigh–Bénard convection for Prandtl numbers between 10^{-1} and 10^4 and Rayleigh numbers between 10^5 and 10^9. *J. Fluid Mech.* **662**, 409–446.

SONG, H., BROWN, E., HAWKINS, R. & TONG, P. 2014 Dynamics of large-scale circulation of turbulent thermal convection in a horizontal cylinder. *J. Fluid Mech.* **740**, 136.

SONG, H., VILLERMAUX, E. & TONG, P. 2011 Coherent oscillations of turbulent Rayleigh-Bénard convection in a thin vertical disk. *Phys. Rev. Lett.* **106** (18), 184504.

SOUCASSE, L., PODVIN, B., RIVIÈRE, P. & SOUFIANI, A. 2019 Proper orthogonal decomposition analysis and modelling of large-scale flow reorientations in a cubic Rayleigh–Bénard cell. *J. Fluid Mech.* **881**, 23–50.

SREENIVASAN, K. R., BERSHADSKII, A. & NIEMELA, J.J. 2002 Mean wind and its reversal in thermal convection. *Phys. Rev. E* **65** (5), 056306.

SUGIYAMA, K., CALZAVARINI, E., GROSSMANN, S. & LOHSE, D. 2009 Flow organization in two-dimensional non-Oberbeck–Boussinesq Rayleigh–Bénard convection in water. *J. Fluid Mech.* **637**, 105–135.

SUGIYAMA, K., NI, R., STEVENS, R. J.A.M., CHAN, T. S., ZHOU, S.-Q., XI, H.-D., SUN, C., GROSSMANN, S., XIA, K.-Q. & LOHSE, D. 2010 Flow reversals in thermally driven turbulence. *Phys. Rev. Lett.* **105** (3), 034503.

SUN, C., XI, H.-D. & XIA, K.-Q. 2005 Azimuthal symmetry, flow dynamics, and heat transport in turbulent thermal convection in a cylinder with an aspect ratio of 0.5. *Phys. Rev. Lett.* **95** (7), 074502.

SUN, C. & XIA, K.-Q. 2005 Scaling of the Reynolds number in turbulent thermal convection. *Phys. Rev. E* **72** (6), 067302.

VERZICCO, R. & CAMUSSI, R. 2003 Numerical experiments on strongly turbulent thermal convection in a slender cylindrical cell. *J. Fluid Mech.* **477**, 19–49.

WAGNER, S. & SHISHKINA, O. 2013 Aspect-ratio dependency of Rayleigh-Bénard convection in box-shaped containers. *Phys. Fluids* **25** (8), 085110.

WANG, Q., XIA, S.-N., WANG, B.-F., SUN, D.-J., ZHOU, Q. & WAN, Z.-H. 2018*a* Flow reversals in two-dimensional thermal convection in tilted cells. *J. Fluid Mech.* **849**, 355–372.

WANG, Y., LAI, P.-Y., SONG, H. & TONG, P. 2018*b* Mechanism of large-scale flow reversals in turbulent thermal convection. *Sci. Adv.* **4** (11), eaat7480.

WANG, Y., XU, W., HE, X., YIK, H., WANG, X., SCHUMACHER, J. & TONG, P. 2018*c* Boundary layer fluctuations in turbulent Rayleigh–Bénard convection. *J. Fluid Mech.* **840**, 408–431.

WEISS, S. & AHLERS, G. 2011*a* The large-scale flow structure in turbulent rotating Rayleigh–Bénard convection. *J. Fluid Mech.* **688**, 461–492.

WEISS, S. & AHLERS, G. 2011*b* Turbulent Rayleigh–Bénard convection in a cylindrical container with aspect ratio $\gamma = 0.50$ and Prandtl number Pr= 4.38. *J. Fluid Mech.* **676**, 5–40.

XI, H.-D., LAM, S. & XIA, K.-Q. 2004 From laminar plumes to organized flows: the onset of large-scale circulation in turbulent thermal convection. *J. Fluid Mech.* **503**, 47–56.

XI, H.-D. & XIA, K.-Q. 2007 Cessations and reversals of the large-scale circulation in turbulent thermal convection. *Phys. Rev. E* **75** (6), 066307.

XI, H.-D. & XIA, K.-Q. 2008*a* Azimuthal motion, reorientation, cessation, and reversal of the large-scale circulation in turbulent thermal convection: A comparative study in aspect ratio one and one-half geometries. *Phys. Rev. E* **78** (3), 036326.

XI, H.-D. & XIA, K.-Q. 2008*b* Flow mode transitions in turbulent thermal convection. *Phys. Fluids* **20** (5), 055104.

XI, H.-D., ZHANG, Y.-B., HAO, J.-T. & XIA, K.-Q. 2016 Higher-order flow modes in turbulent Rayleigh–Bénard convection. *J. Fluid Mech.* **805**, 31–51.

XI, H.-D., ZHOU, S.-Q., ZHOU, Q., CHAN, T.-S. & XIA, K.-Q. 2009 Origin of the temperature oscillation in turbulent thermal convection. *Phys. Rev. Lett.* **102** (4), 044503.

XIA, K.-Q. 2013 Current trends and future directions in turbulent thermal convection. *Theor. Appl. Mech. Lett.* **3** (5), 052001.

XIA, K.-Q., SUN, C. & ZHOU, S.-Q. 2003 Particle image velocimetry measurement of the velocity field in turbulent thermal convection. *Phys. Rev. E* **68** (6), 066303.

XIAO, Y, TAO, J.-J., MA, X. & XIONG, X.-M. 2018 Oscillating convection and reversal flow in connected cavities. *Phys. Rev. E* **98**, 063109.

XU, A., SHI, L. & XI, H.-D. 2019*a* Lattice Boltzmann simulations of three-dimensional thermal convective flows at high Rayleigh number. *Int. J. Heat Mass Transf.* **140**, 359–370.

XU, A., SHI, L. & XI, H.-D. 2019*b* Statistics of temperature and thermal energy dissipation rate in low-Prandtl number turbulent thermal convection. *Phys. Fluids* **31** (12), 125101.

XU, A., SHI, L. & ZHAO, T.S. 2017*a* Accelerated lattice Boltzmann simulation using GPU and OpenACC with data management. *Int. J. Heat Mass Transf.* **109**, 577–588.

XU, A., SHYY, W. & ZHAO, T. 2017*b* Lattice Boltzmann modeling of transport phenomena in fuel cells and flow batteries. *Acta Mech. Sin.* **33** (3), 555–574.

ZHANG, Y., ZHOU, Q. & SUN, C. 2017 Statistics of kinetic and thermal energy dissipation rates in two-dimensional turbulent Rayleigh–Bénard convection. *J. Fluid Mech.* **814**, 165–184.

ZHOU, Q. & XIA, K.-Q. 2010 Physical and geometrical properties of thermal plumes in turbulent Rayleigh–Bénard convection. *New J. Phys.* **12** (7), 075006.

ZHOU, S.-Q., SUN, C. & XIA, K.-Q. 2007 Measured oscillations of the velocity and temperature fields in turbulent Rayleigh-Bénard convection in a rectangular cell. *Phys. Rev. E* **76** (3), 036301.

ZHOU, W.-F. & CHEN, J. 2018 Similarity model for corner roll in turbulent Rayleigh-Bénard convection. *Phys. Fluids* **30** (11), 111705.